Neuron, Volume *80*

Supplemental Information

Dissecting Local Circuits:

Parvalbumin Interneurons Underlie Broad

Feedback Control of Olfactory Bulb Output

Kazunari Miyamichi, Yael Shlomai-Fuchs, Marvin Shu, Brandon C. Weissbourd, Liqun Luo, and Adi Mizrahi

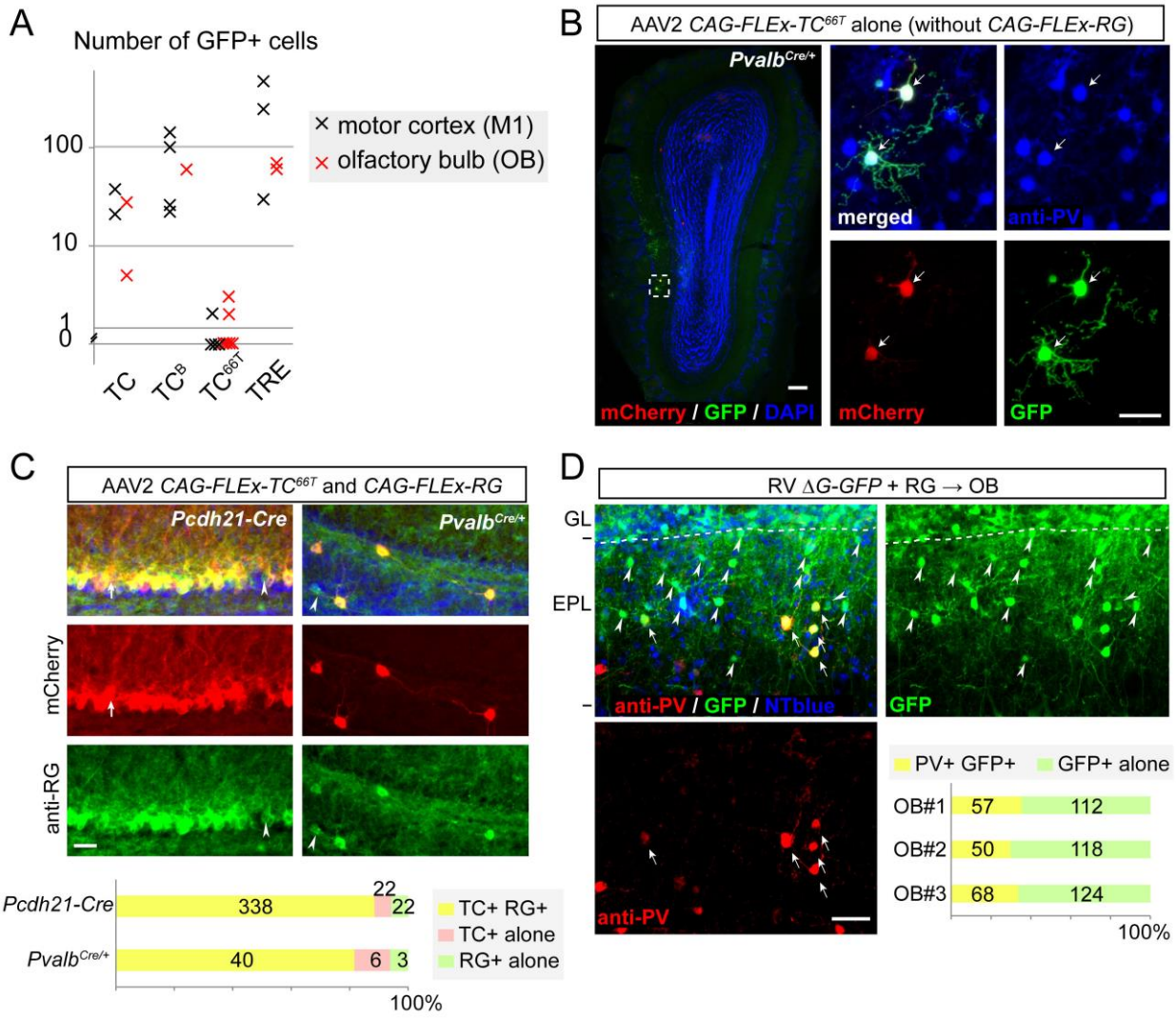

Figure S1. Additional Control Experiments for Cell Type-Specific Transsynaptic Labeling, Related to Figure 1.

(A) Estimating non-specific labeling by RV due to leaky TVA expression. Quantification of GFP+ cells in experiments with wild-type mice using AAV2 *EF1a-FLEx-TC* (Watabe-Uchida et al., 2012), *CAG-FLEx-TC*^{B}, *CAG-FLEx-TC*^{66T} and *TRE-HTG* (Miyamichi et al., 2011). Because the TVA receptor is highly sensitive to EnvA-pseudotyped rabies virus (Seidler et al., 2008; Wall et al., 2010), a small amount of leaky expression of TVA from Cre-dependent viruses in the absence of Cre (Wall et al., 2010; Watabe-Uchida et al., 2012), or tTA2-dependent viruses in the absence of tTA2 (Miyamichi et al., 2011), can cause non-specific initial infection of the RV. The density of this non-specific labeling can vary by brain regions and by the titer of AAV and RV. Indeed, when we used higher titer RV and AAV in the tTA2/TRE-based strategy, we found >10-fold non-specific labeling of RV in the local injection site than we previously reported (Miyamichi et al., 2011). Therefore, we compared side-by-side four different strategies in the neocortex of wild-type mice to assess the Cre or tTA2 independent non-specific rabies labeling. The numbers of RV labeled cells in wild-type animals are plotted, with each cross (black, motor cortex; red, olfactory bulb) representing

one independent experiment. Only *TC*^{66T}-based strategy has nearly 0 non-specific labeling.

(B) Testing RG-dependency of transsynaptic RV spread. AAV2 *CAG-FLEx-TC*^{66T} alone (without *CAG-FLEx-RG*) was injected into the olfactory bulb (OB) of *Pvalb*$^{Cre/+}$ mouse (Hippenmeyer et al., 2005). Two week later, RV *ΔG-GFP*+EnvA was injected into the same area. A single 60-μm coronal section stained with anti-PV antibodies is shown. 20±2.6 GFP+ neurons (n=3 animals) were found near the injection site, and all of them were labeled with mCherry and anti-PV (indicated by arrows), demonstrating that our AAV *FLEx* vector is specifically activated in the Cre-positive neurons *in vivo*. Importantly, in the absence of AAV *CAG-FLEx-RG*, RV transduction was almost completely limited to the mCherry+ populations. Non-specific GFP expression outside the mCherry+ population was 2±0.6 cells per animal (n=3), which is within the range of Cre-independent labeling in the wild-type control (panel A, *TC*^{66T}). These data confirmed that transsynaptic spread of RV strictly depends on the function of RG. Scale bars, 100 μm for the left panel; 25 μm for the right four panels.

(C) Testing co-transduction efficiency of AAV2 *CAG-FLEx-RG* and AAV2 *CAG-FLEx-TC*^{66T}. Because RG and TC (TVA-mCherry) are driven by two independent AAVs (Watabe-Uchida et al., 2012), some neurons may receive only one of these two AAV vectors. RG–/TC+ neurons can receive EnvA pseudotyped RV and therefore are indistinguishable from the starter cells, but cannot produce infectious RV due to the lack of RG (we term these pseudo-starter cells). RG+/TC– neurons can trans-synaptically receive RV if they are the presynaptic partners of one of the starter cells, and can generate infectious RV, even though they are not labeled with mCherry (we term these invisible starter cells). To test the abundance and distribution of pseudo-starter cells and invisible starter cells, we injected into *Pcdh21-Cre* (n=3) and *Pvalb*$^{Cre/+}$ (n=3) a 1:1 mixture of *CAG-FLEx-RG* and *CAG-FLEx-TC*^{66T} and stained sections with anti-RG antibodies. Within 400 μm around the injection site, 88.6% (*Pcdh21-Cre*) and 81% (*Pvalb*$^{Cre/+}$) of labeled neurons were dually labeled with TC and RG. As starter cells tend to cluster near the injection site, these data indicate that most of our TC+ cells are bona fide starter cells. RG+/TC– (indicated by arrowheads) or RG–/TC+ (indicated by arrows) were a minority near the injection site, although RG–/TC+ neurons were sometimes more broadly distributed than RG+/TC– neurons. Thus, pseudo-starter cells may be present in the periphery of the injection site, and this could lead to an over-estimate of the spatial spread of the starter cells in our experiments. Scale bar, 25 μm.

(D) To test if non-PV neurons in the EPL (Huang et al., 2013; Lepousez et al., 2010) are competent to receive RV, we made use of the in vitro complemented RV *ΔG-GFP*+RG. This virus can infect cells that would be infected by the wild-type RV but cannot produce further viral particles for transsynaptic transmission (Miyamichi et al., 2011; Wickersham et al., 2007). 0.3μl of RV *ΔG-GFP*+RG was injected into the lateral surface of the OB (n=3), and EPL neurons were analyzed 4 days later. A typical example of a 60-μm coronal section near the injection site is shown. In total, 33±1.6% GFP+ neurons in the EPL were co-stained with anti-PV antibodies (arrows), while many non-PVNs were labeled with GFP (arrowheads). This is markedly different from transduction of cells

trans-synaptically from M/T cells (Figure 2B), where 88±1.6% GFP+ neurons were PVNs ($p<0.001$, t-test). Thus, transsynaptic RV spread specifically labeled a sub-population of all RV competent neurons in EPL, supporting synaptic specificity of RV spread in vivo. Scale bar, 25 μm.

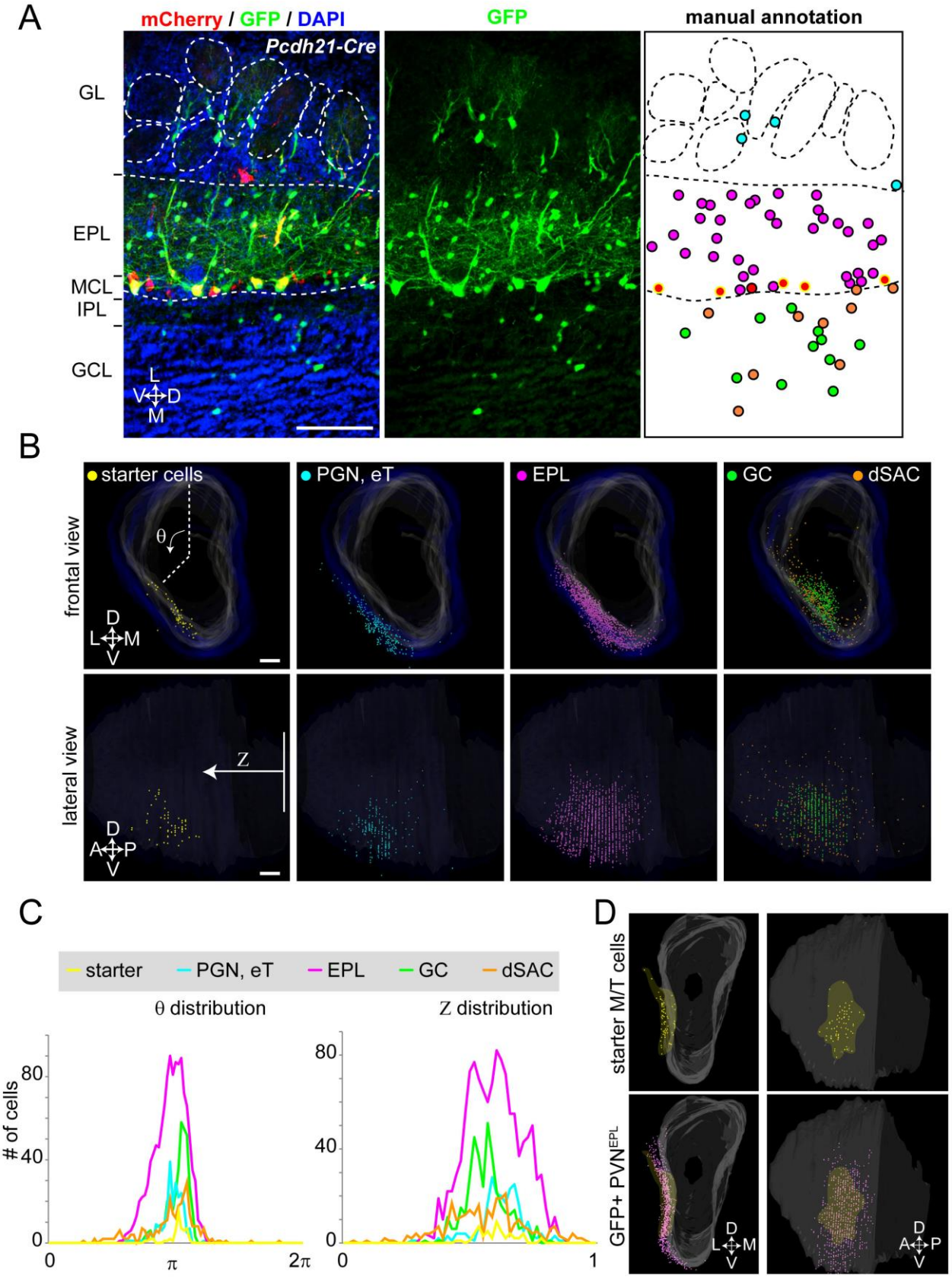

Figure S2. 3D Reconstruction of the Labeled OB Samples, Related to Figure 2.

(A) A typical 60-μm OB section with five starter MCs and many GFP+ neurons. After detecting the

mitral cell layer and the boundary between the glomerular layer and EPL, we manually annotated starter cells (with a yellow contour) and GFP-labeled presynaptic neurons in different layer and/or of different cell types with differently colored circles (GL, cyan; EPL, magenta; MC, red; GC, green; and dSAC, orange). A custom-made MATLAB program automatically assembles these manual annotations to form 3D reconstructions (see Supplemental Experimental Procedures for details). Scale bar, 100 μm.

(B) Frontal (top panels) and lateral (bottom panels) views of a 3D reconstructed OB model from a *Pcdh21-Cre* tracing experiment. White shadow represents the mitral cell layer, and the blue shadow represents the boundary between the GL and EPL. In this sample, 51 starter MCs and 3 starter external tufted cells (eTs) were found in the ventro-lateral area of the OB (yellow dots). 465 GFP+ neurons in GL are shown in cyan dots, which contain periglomerular cells (PGNs) and eTs. 1225 GFP+ cells in the EPL (magenta), 380 GCs (granule cells, green) and 302 dSACs (deep short axon cells, orange) are also shown side by side. As shown in Figure 2C and 2D, the labeled dots were quantified in the cylindrical coordinate system (θ for the rotation angle from the dorsal polar axis, *Z* for the distance from the most posterior section). Scale bar, 100 μm.

(C) Histograms showing the distribution of θ and *Z* for each group (colors of the line in the histogram match the colors of the dots in panel A and B).

(D) Another 3D-reconstucted OB model from a different *Pcdh21-Cre* tracing sample, where 53 external tufted cells and 14 MCs were identified as starter cells (shown in yellow). As in Figure 2C, we stained every section form this sample with anti-PV antibody and identified 752 (out of 855 GFP+ EPL cells, 88%) were $PVNs^{EPL}$ (shown in magenta). Areas of starter cells are highlighted by yellow shadows.

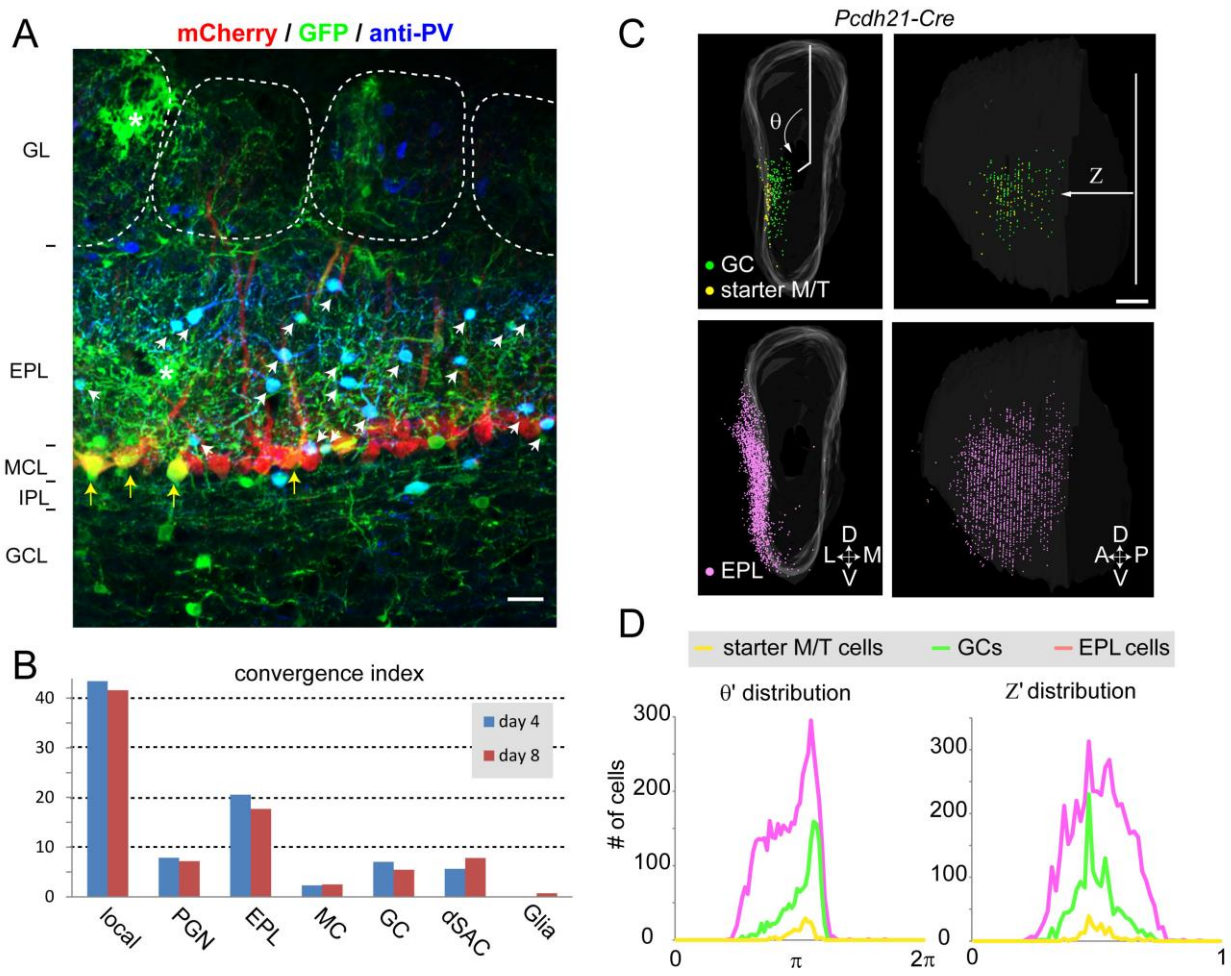

Figure S3. Longer Survival Period After RV Infection Does Not Change Labeling Patterns, Related to Figure 2.

(A) To test if a longer survival period alters the pattern of transsynaptic spread of RV, we used the *CAG-FLEx-TC*^{66T}-based transsynaptic tracing strategy in *Pcdh21-Cre* mice (as in Figure 2) and waited for 8 days after RV injection instead of the 4 days used for data described for all other experiments. We obtained two samples, with a total of 272 starter M/Ts and 11,317 local GFP+ cells across all layers of the OB. Shown here is a typical 60-µm coronal OB section stained by anti-PV antibodies containing starter MCs (yellow arrows) and GFP+ presynaptic neurons. GL, glomerular layer; EPL, external plexiform layer; MCL, mitral cell layer; IPL, internal plexiform layer; GCL, granule cell layer. Neurons co-labeled with GFP and anti-PV antibodies in the EPL are indicated by white arrows. Glial processes are indicated by asterisks. Scale bar, 20 µm.

(B) The convergence indices (the number of GFP+ cells divided by the number of starter cells) for the pooled day 4 and day 8 samples. Length of survival period did not change the convergence indices or layer distributions of GFP+ cells. Notably, we detected a significant number of glia cells only in day 8 samples.

(C) Frontal (left panels) and lateral (right panels) views of a 3D reconstructed OB model of a day 8

sample. In this sample, we found 50 starter MCs (yellow, top panels), 169 putative pre-synaptic GCs (green, top panels), and 1,809 putative pre-synaptic neurons in the EPL (magenta, bottom panels). As we observed in Figure 7C and Figure S2, GFP+ GCs clusters are close to starter MCs. In contrast, GFP+ cells in the EPL were more broadly distributed than starter MCs, as we observed in day 4 samples (Figure S2B, C).

(D) Histograms showing the distribution of normalized and pooled θ' and Z' values for each group in the 8-day experiment (the colors of the lines in the histogram match the colors of the dots in panel C).

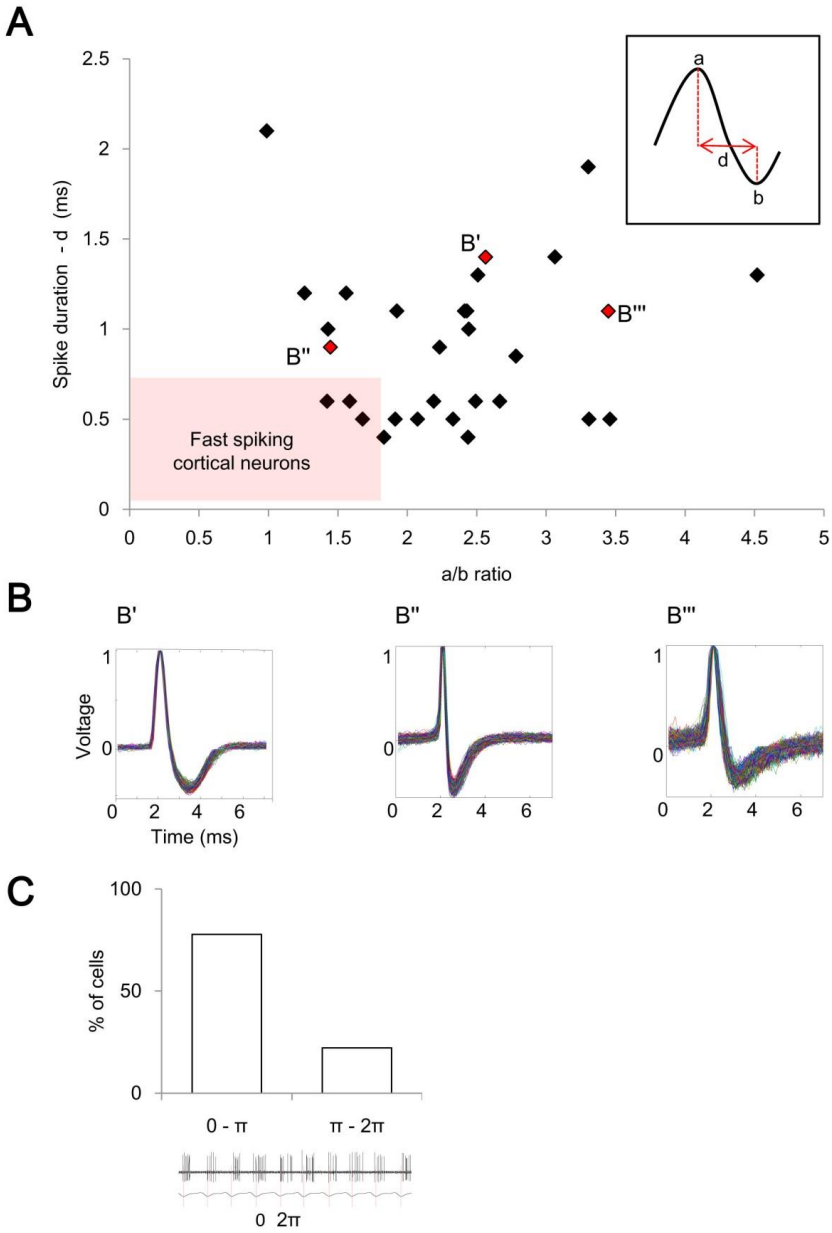

Figure S4. Spontaneous Electrophysiological Properties of PVN^{EPL}, Related to Figure 3.

(A) The spike waveforms of all PVN^{EPL} in our data set were characterized by spike peak (a, inset) to volley (b, inset) ratio relative to spike peak to volley duration (d, inset). Red area indicates the threshold for waveform characteristics of cortical fast spiking neurons.

(B) Examples of the spike waveform of 3 different PVN^{EPL} denoted B'-B''' in A. Colored lines represent individual spike waveforms, dashed black line represents mean waveform.

(C) Spontaneous phase tuning of PVN^{EPL}. Top, histogram of the spontaneous phase tuning of PVN^{EPL}. Bottom, raw spiking traces of spontaneous activity shown with regard to the respiration. Red lines mark the start (0) and end (2π) of one respiration cycle.

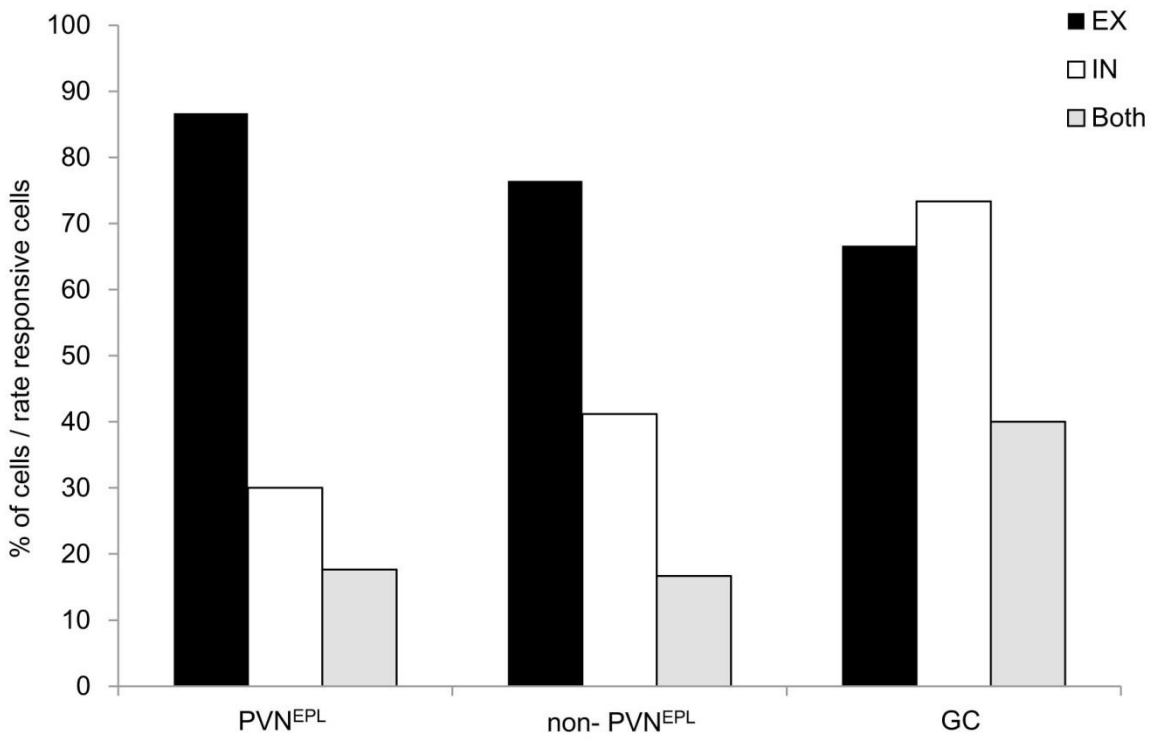

Figure S5. Most PVNs Show Exclusively Excitatory or Exclusively Inhibitory Odor-Evoked Responses, Related to Figure 5.

Histogram of the percentage of cells responding with inhibition, excitation or both, for all cell groups. Only cells that showed changes in spike rates are included.

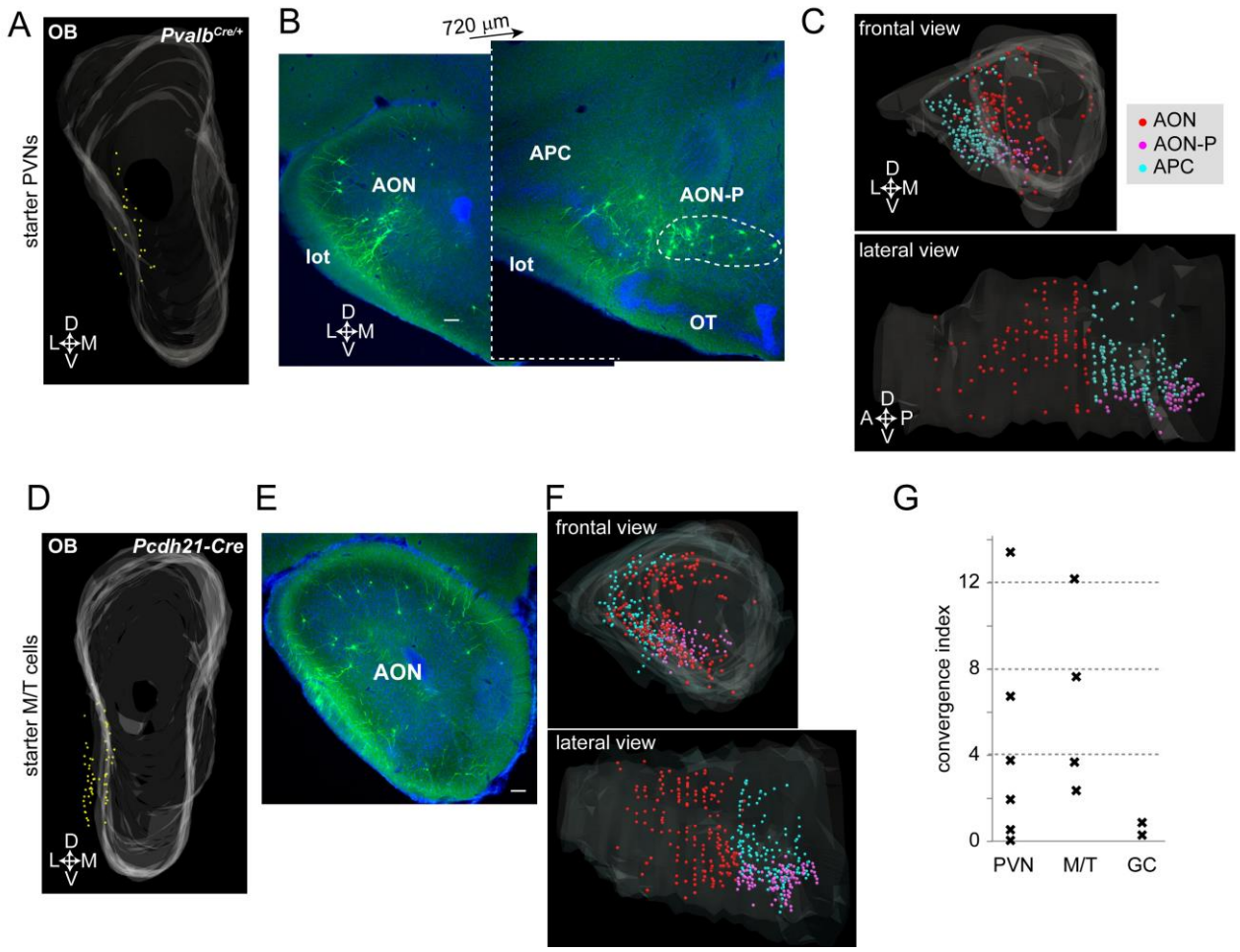

Figure S6. Cortical Feedback Projections to PVNs and Mitral/Tufted Cells in the OB, Related to Figure 2 and Figure 6.

(A) A 3D-reconstructed *Pvalb*$^{Cre/+}$ OB sample showing starter PVNs (21 PVNs^{IPL} and 3 PVNs^{EPL}) in the ventro-lateral part of the OB. In this sample, 101 GFP+ neurons were found in the anterior olfactory nucleus lateral, dorsal, and ventral division (hereafter referred to as AON for simplicity), 61 GFP+ neurons were found in AON posterior division (AON-P) (Brunjes et al., 2005), and 164 GFP+ neurons were identified in the anterior piriform cortex (APC). These observations indicate that PVNs in the OB directly receive cortical feedback projections.

(B) Typical examples of single 60-μm sections containing GFP+ AON and APC cortical neurons. OT, olfactory tubercle; lot, lateral olfactory tract. Scale bar, 100 μm.

(C) To visualize the spatial distribution of GFP+ neurons in the AON/APC, we used a previously established custom-made 3D-reconstruction program (Miyamichi et al., 2011). GFP+ neurons are shown as colored dots according to the location of their cell bodies, in the frontal (top) and lateral (bottom) views. White surface represents the boundary between layer I and layer II of the AON and APC. The GFP+ neurons were distributed broadly throughout the AON and anterior APC, suggesting a lack of apparent topographic organization of cortical feedback projections to the PVNs in the OB.

Data presented in panel (A-C) are originated from the same animal.

(D) A 3D reconstructed *Pcdh21-Cre* OB sample showing starter M/T cells (the same as Figure 2C) in the ventro-lateral part of the OB. In this sample, 181 AON neurons, 100 AON-P neurons, and 166 APC neurons were GFP+, suggesting direct cortical feedback input to the M/T cells.

(E) A representative example of a single 60-μm section containing GFP+ AON cortical neurons. Scale bar, 100 μm.

(F) Spatial distribution of GFP+ neurons in AON/APC, as in the panel (C). Data presented in panel (D-F) originated from the same animal.

(G) Convergence index (defined by the number of GFP+ cortical neurons divided by the number of starter OB neurons) is plotted for the three different starter cell populations in the OB: PVN by $Pvalb^{Cre/+}$ (Figure 6), M/T cells by *Pcdh21-Cre* (Figure 2), and GC by $GAD2^{Cre/+}$ (Figure 7).

Supplemental Experimental Procedures

Constructs and Virus Preparations

CAG-FLEx-RG, *CAG-FLEx-TC*^{B}, and *CAG-FLEx-TC*^{66T} cassette were constructed using standard molecular cloning methods with enzymes commercially available from New England Biolabs (Ipswich, USA). Specifically, the 330-base pair synthesized DNA fragment shown below was obtained from DNA 2.0 (Menlo Park, USA). This DNA fragment contained restriction enzyme sites and two heterospecific pairs of loxP (shown by underline) and *lox2272* (shown by italic) in the following order:

NotI-MluI-XmaI-*lox2272(c)*-loxP(c)-SalI-AscI-*lox2272*-loxP-HindIII-SpeI-NotI.

5’-GCGGCCGCACGCGTAATTCCCGGG*ATAACTTCGTATAAAGTATCCTATACGAAGTTAT*ATCA
AAATAGGAAGACCAATGCTTCACCATCGACCCGAATTGCCAAGCATCACCATCGACACAT
AACTTCGTATAATGTATGCTATACGAAGTTATGTCGACATATGGCGCGCCT*ATAACTTCGTAT*
*AGGATACTTTATACGAAGTTAT*CATTGGGATTCTTCCTATTTTGATCCAAGCATCACCATCGAC
CCTCTAGTCCAGATCTCACCATCGACCCATAACTTCGTATAGCATACATTATACGAAGTTAT
AAGCTTAATTACTAGTGCGGCCGC-3’

After cloning this DNA fragment into the modified *pBluescript* vector that only contains a NotI site in the cloning site, the following DNA fragments were sub-cloned by using the unique restriction sites.

1) A DNA fragment containing the *WPRE* sequence and transcription termination signal from human growth hormone gene (*hGHpA*) was obtained from *pAAV-TRE-HTG* plasmid (Miyamichi et al., 2011) by using HindIII and SpeI restriction enzymes.
2) A DNA fragment containing the *CAG* promoter flanked by PstI (blunt ended by Klenow fragment) and XmaI sites was obtained from plasmid *pCA-G-intron-T* (Tasic et al., 2012). MluI (blunt ended by Klenow fragment) and XmaI sites in our vector were used for sub-cloning.

3-1) A PCR fragment was amplified using Phusion Taq polymerase from *pAAV-CAG-FLEX-RG* and *pAAV-EF1a-FLEX-TVA-mCherry* (Watabe-Uchida et al., 2012). The following primers including a Kozak sequence (underlined) before the initiation codon (italic) were used:
For the *RG* cassette,
5’-GGCGCGCCACC*ATG*GTTCCTCAGGCTCTCCT:
5’- GTCGACTTACAGTCTGGTCTCACCCC
For *TC*^{B} cassette,
5’-GGCGCGCCACC*ATG*GCGCGGCTGCTGCCCGC:
5’-GTCGACTTACTTGTACAGCTCGTCCA
These cassettes were flanked by AscI and SalI.

3-2) The *TC*^{66T} cassette was produced using PCR based introduction of the point mutation into the TVA receptor. Note that the point mutation in our vector (E66^{T}) corresponds to the E47^{T} mutation in the TVA800 (Rong et al., 1998). A part of TVA receptor gene was amplified with

the point mutation (GAG→ACC) by Phusion Taq polymerase using the plasmid *pAAV-EF1a-FLEX-TVA-mCherry* (Watabe-Uchida et al., 2012) as a template. This PCR product (208 base pairs) also contains the restriction site AscI, and the kozak sequence (underlined) located immediately upstream of the initiation codon (italic). The following PCR primers were used.:

5'-GGCGCG<u>CCACC</u>*ATG*GCGCGGCTGCTGCCCGC:

5'-**GGT**GTCCCGCCCGTCGTCGCAGT

The rest of the sequence for the TVA receptor fused with mCherry was amplified from the same template *pAAV-EF1a-FLEX-TVA-mCherry* using the following PCR primers:

5'-GCGACGACGGGCGGGAC**ACC**TGGGGCTGCGGGACCAGCGC:

5'-GTCGACTTACTTGTACAGCTCGTCCA.

These two PCR products were then mixed together and used as a template to obtain the full length TC^{66T} cassette flanked by AscI and SalI restriction sites by using the PCR primers:

5'-GGCGCG<u>CCACC</u>*ATG*GCGCGGCTGCTGCCCGC.

5'-GTCGACTTACTTGTACAGCTCGTCCA.

The assembled cassettes were sub-cloned into *pAAV-MCS* (AAV helper free system, Stratagene, Cat#240071-12) using the NotI site. The final constructs *CAG-FLEx-*TC^{B}, and *CAG-FLEx-*TC^{66T} were tested by transient transfection into cultured HEK293 cells, using *EF1a-FLEx-TC* as a reference (Figure 1). Using 6-well plates, 1.5μg of the each circular plasmid, with or without 1.5μg of a Cre-encoding plasmid *pBT140* (*CMV* promoter driving nuclear localization signal-*Cre*), was introduced into the HEK293 cells using Lipofectamine 2000 (Invitrogen, Cat#11668-027) according to the manufacture's instructions. Fluorescence of mCherry was detected 72 hours post-transfection.

All viral procedures followed the Biosafety Guidelines approved by the Stanford University Administrative Panel on Laboratory Animal Care (A-PLAC) and Administrative Panel of Biosafety (APB). Recombinant AAV vectors (serotype 2) were produced in the Stanford Viral Core. The AAV titer was estimated to be 1.6, 5.6, and 2.8 x 10^{11} viral particles/ml for *CAG-FLEx-RG*, *CAG-FLEx-*TC^{B}, and *CAG-FLEx-*TC^{66T}, respectively, based on quantitative PCR analysis. Pseudotyped *ΔG* RV was prepared as previously described (Wickersham et al., 2007; Wickersham et al., 2010). The pseudotyped RV titer was estimated to be ~5 x 10^{9} infectious particles/ml based on serial dilutions of the virus stock followed by infection of the 293-TVA800 cell line.

Two-Photon Targeted Recording from PV-Positive Neurons

Imaging of the OB was performed using an Ultima two-photon microscope from Prairie Technologies (Middleton, WI), equipped with a 16X water-immersion objective lens (0.8 NA;CF175, Nikon). Two-photon excitation of the electrode and somata was used at 915nm (DeepSee femtosec laser, Spectraphysics) and the laser beam was extended to fill the large back aperture of the 16X objective.

Electrodes (5-10 MΩ) were pulled from filamented, thin-walled, borosilicate glass (outer

diameter, 1.5 mm; inner diameter, 1.0 mm; Hilgenberg GmbH, Malsfeld, Germany) on a vertical two-stage puller (PC-12, Narishige, EastMeadow, NY). Electrodes were filled with an internal solution containing (in mM): 140 K-gluconate, 10 KCl, 10 HEPES, 10 Na_2-Phosphocreatine, 4 MgATP, 0.4 Na_2GTP, 0.5 EGTA, pH adjusted to 7.25 with KOH. For electrode visualization the internal solution was supplemented with 200 µM Alexafluor 488 (Life technologies, Invitrogen). To minimize brain pulsations two percent low melting agar (type IIIa, Sigma-Aldrich, St. Louis, MO) was placed over the craniotomy. All recordings were acquired using an intracellular amplifier in current clamp mode (Multiclamp 700B, Molecular Devices), at a sampling rate of 10 kHz (Digidata 1440A, Molecular Devices, Sunnyvale, CA), and were filtered using a 50 Hz high pass filter. Recordings from $PVNs^{EPL}$ and non-PVN^{EPL} were made strictly from the EPL (mean recording depth 186.76±42.13µm), and GC's were targeted by limiting the patch pipette depth to the GCL (i.e. >340µm; Figure 4A). Recording locations were widely distributed across the dorsal part of the OB, to minimize potential bias from sampling a spatially restricted population.

The electrode was directed toward the cells under visual guidance, to achieve loose patch configuration. Lateral excursions of the electrode were kept to distances less than 100 µm. Correct targeting was initially verified by visual guidance, and an increase in electrode resistance. Additionally, fluorescent dye from the electrode was electroporated into the cell using current pulses. Only tdTomato+ cells that were distinctly filled during this procedure were included in our dataset.
For the control group of non-PVN^{EPL} cells, data was collected either by shadow patching (Kitamura et al., 2008) or by "blind" patching in the vicinity of tdTomato+ cells. Non-PVN^{EPL} cells were also filled after recording.

Respiration-Triggered Odor Delivery

Odor stimuli were delivered directly to the nose via a custom made 5-channel olfactometer with completely isolated odor channels to circumvent contamination between odors.

Upon odor delivery, the N_2 stream was switched into one of the odor vials for the desired duration, while the overall flow was kept constant. A custom-written MATLAB program controlling a Master-8 (A.M.P.I, Israel) was used to control the odor delivery from the olfactometer. A panel of 5 odors known to activate the dorsal part of the OB were used in all experiments (Luo and Katz, 2001; Reidl et al., 2007; Soucy et al., 2009). The odors (butanal, pentanal, ethyl tiglate, propanal and ethyl butyrate) were all obtained from Sigma-Aldrich. We limited the duration of our odor protocol to ~20 minutes, and to increase statistical power we used 4-10 trials/odor. The odors were presented for 2 secs, in pseudo-random order, with an inter-stimulus interval of 18 secs. Odors were first diluted in mineral oil according to their individual vapor pressures to give a nominal headspace concentration of 1000 ppm. Next, odors were further diluted with O_2 to achieve a final concentration of 50 ppm or 500 ppm. No significant differences between the average data of these concentrations were found so odor concentrations were pooled.

The animal's respiration was monitored throughout the experiment by a low pressure sensor

(1-INCH-D1-4V-MINI, by 'All sensors'). The low pressure sensor was connected to a thin stainless steel tubing (OD 0.7 mm) which was placed at the entrance of the animals' contra-lateral nostril. The information from the pressure sensor was passed to an analogue converter (window discriminator), which was used to identify the inhalation onset during the respiratory cycle. We then used a custom-written MATLAB program to trigger odor delivery at inhalation onset.

Electrophysiology Data Analysis

A custom-written MATLAB program was used to perform data analysis. Spikes were extracted from voltage traces using thresholding. Spike times were assigned to the local peaks of supra threshold segments and rounded to the nearest msec. Respiration cycle times were calculated by finding local minima and maxima in the respiration trace.

Throughout all trials, spontaneous firing rate was assessed by calculating the mean spontaneous firing rate based on the 4 secs period that preceded each stimulus. Spontaneous phase tuning was assessed by first assigning each spike its timing in the respiration cycle (0-2π), during the 2 secs preceding odor stimulation. Next, the cell's temporal spiking pattern was examined to determine whether it is significantly tuned to a certain phase in the respiration cycle, or is uniformly distributed throughout the cycle. In order to test for circular uniformity the Rayleigh test was used (Berens, 2009), significant phase tuning was accepted at $p<0.01$. For significantly phase-tuned cells the mean angular direction of the spikes was calculated, as the phase in the respiration cycle to which the cell was tuned. Spike waveform of PVN^{EPL} was extracted and average spike waveform calculated using a custom-written MATLAB program. Using the average spike waveform two parameters were calculated: spike duration (between spike peak to volley) and the ratio between the amplitudes of the spike peak and volley (Cohen et al., 2011; McCormick et al., 1985; Niell and Stryker, 2008) (Figure S4).

Odor responses were defined as either changes in spike rate or changes in the angular distribution of spikes in the respiration cycle (changes in phase tuning), or both (e.g. Figure 5A- rate changes; 5B,C- phase tuning changes). Changes in spike rate were detected by comparing: (1) The mean firing rate in the 2 sec preceding odor onset to the mean firing rate during the entire 2 sec odor period, across all repetitions of the same odor. (2) The mean firing rate in the 2 sec preceding odor onset to the 2 sec after odor offset, across all repetitions of the same odor. (3) The average spike rate per respiration during the 2 secs preceding odor onset to the spike rate in each respiration during the odor period, across all repetitions of the same odor. For these comparisons a paired T-test was used, accepting significance at $p<0.05$, except for the analysis of single respirations, in which case the Bonferroni correction for multiple comparisons we applied. Phase tuning responses were analyzed only if a cell showed significant phase tuning before and during the odor presentation. Phase tuning responses were detected by comparing the cell's phase tuning in the 2 secs preceding odor onset to the phase tuning during the 2 secs odor period, across all trials. For this comparison a multi-sample test for equal median directions was used (Berens, 2009).

Odor rate responses were classified as either excitatory (increase in spike rate) or inhibitory (decrease in spike rate). An odor response was considered inhibitory only if it was not preceded by an excitatory response, and *vice versa*. The percentage of excitatory versus inhibitory responses was calculated out of the total number of odor evoked changes in firing rate. Response magnitude was calculated as the absolute maximal change in firing rate either during the entire odor presentation or per respiration, across odors.

For the comparison of multiple groups, a one way ANOVA was used (significant accepted at $p<0.01$) followed by post hoc pair-wise comparisons using Tukey's honestly significant difference criterion (Tukey's HSD, confidence interval 95%).

Significant differences between the percentages of cells/responses of different categories between groups were tested using a test for comparison of the proportions of two binomial variables (e.g. the percentage of excitatory versus inhibitory responses, Fig 5E).

Immunohistochemistry and Microscopy

For transsynaptic tracing experiments (Figure 1, 2, 6, and 7) brain tissue was processed according to previously described procedures (Espinosa et al., 2009; Miyamichi et al., 2011). To set the common coronal plane among different animals, the cerebellum was cut off, and the brain was embedded in the Optimum Cutting Temperature (O.C.T.) compound (Tissue-Tek) with the cutting surface facing the bottom of the mold. The brain was adjusted to ensure that the left-right axis was parallel to the section plane. Neither mCherry nor GFP required immunostaining for visualization. The following antibodies were used in the analysis of cell type of starter cells and trans-synaptically labeled neurons: rabbit anti-parvalbumin (1:2000, Swant), rabbit anti-tyrosine hydroxylase (1:500, Millipore, Cat#ab152), rabbit anti-calretinin (1:500, Abcam, Cat#ab702), rabbit anti-Tbr2 (1:500, Abcam, Cat#ab23345), and mouse anti-rabies glycoprotein (1:500, Millipore, Cat#mab8727). 60μm, free floating, coronal sections of the OB were treated for 1 hour at room temperature with 5% normal goat serum in phosphate buffer serine containing 0.3% Triton-X1000 (PBST). Tissues were then treated at 4 degrees free floating with primary antibodies in 0.3% PBST for 4 days. After washing three times for 10 min with 0.3% PBST, the sections were treated with goat anti-rabbit Alexa Fluor 647 or goat anti-mouse Alexa Fluor 488 (1:200, Jackson ImmunoResearch) at 4 degree for 2 days, followed by washing three times for 10 min with 0.3% PBST. Finally the sections were treated with PBS containing 4',6-diamidino-2-phenylindole dihydrochloride (DAPI; Sigma, Cat#D8417) or NeuroTrace Blue (1:500, Invitrogen, Cat#N-21479) for 20 min and mounted with cover glass using Fluorogel (Electron Microscopy Sciences, Cat#17985-10) Sections were imaged with a Nikon CCD camera by using a 10x objective or by 1.6-2.0 μm optical sectioning using confocal microscopy (Zeiss 510 or 780).

For Figure 3A, coronal sections (40μm) of the OB were treated with anti-PV antibodies (Swant, rabbit anti-PV, 1:1000 in blocking solution) overnight, washed with PBS, and then incubated for another 2 hours with a secondary antibody (Chemicon, goat anti-rabbit-Cy5, 1:250). Slices were

imaged by Leica SP50 confocal microscope (Wetzlar, Germany), equipped with a 40X (1.25 NA) Leica oil objective (Wetzlar, Germany). Counting of neuronal somata was performed manually from the confocal images by choosing random regions of the EPL within the slices. Each somata was scored as labeled with tdTomato, Cy5, or both.

3D-Reconstruction and Quantitative Analysis.

The 3D-reconstruction and cylindrical coordinate systems for the OB and AON/APC were previously described (Miyamichi et al., 2011). To adjust the established programs for the current study, the following additions and modifications were made.

1) We generated a semi-automatic system to detect the MCL and EPL/GL boundary in each coronal section of the OB by processing the density distribution of the DAPI signal. For this, we utilized the fact that DAPI signal is significantly higher in the MCL and in the GL than in the EPL. To process an image of an OB section, we first removed background noise and performed Gaussian blurring of the DAPI signal. Next, DAPI signal intensity was measured along each radiation axis of the OB (a ray starting from the center of the OB and extending outwards) at 1 degree intervals. The DAPI intensity moving along each radiation angle would be high in the GCL/MCL, drop in the EPL, and rise again in the GL. Therefore, when DAPI intensity is plotted along each radiation angle, the first falling edge corresponds to the MCL and the subsequent rising edge corresponds to the EPL/GL boundary. The MATLAB processing detected these boundary points, and in addition, tracked the boundary points that were detected at neighboring radiation angles to check that the detected boundaries remained continuous. The MCL and EPL/GL boundary were thereby marked by a dense series of points, which were then recorded into Scalable Vector Graphics (SVG) format. The entire process was implemented in a MATLAB program that ran automatically with human correction when necessary.
2) After plotting the MCL and EPL/GL boundary, we manually annotated starter cells and GFP-labeled presynaptic neurons using dots of different colors to represent cells of different layers and types. This manual annotation was carried out in Adobe Illustrator and stored in an SVG file, which was read by MATLAB. We used the mass center for all dots that corresponded to the MCL and EPL/GL layers to approximate a single point representing the mass center of a slice. The precise slice centering and rotation, assembly of multiple slices, and setting the polar axis were performed as previously described (Miyamichi et al., 2011). The only modification is that instead of aligning complete glomeruli between slices, the EPL/GL boundary was used for alignment. These two methods give similar results. All steps after manual annotation of GFP labeled cells were automatically done by MATLAB without human intervention to avoid biasing the registration results. These MATLAB scripts are available upon request.
3) For AON/APC reconstruction (figure S6), we increased the number of colors during the manual annotation of labeled cells such that neurons in the different anatomical structures (e.g., AON or APC) can be mapped by distinct colors.

We used Paraview (version 3.98) to visualize the Visualization Toolkit (VTK) format file of 3D reconstructed OB and AON/APC.

For the distribution of θ and Z analysis, we pooled θ and Z values from multiple experiments as individual samples contained relatively small number of starter cells for the statistical analysis. Because location of starter cells was slightly different between the each sample, we normalized the data by a uniform transformation to each OB such that the median $\theta_{starter}$ and median $Z_{starter}$ turn to an identical value among multiple samples. In *Pcdh21-Cre* experiments (Figure 2D, 7D), median $\theta_{starter}$= 0.96 ± 0.03 π and median $Z_{starter}$ = 0.63 ± 0.047 (n=3 animals) were normalized to $\theta'_{starter}$ = 1.00π and $Z'_{starter}$ = 0.600, respectively. In the *PV-Cre* experiments (Figure 6D), median $\theta_{starter}$ = 0.92 ± 0.025 π and median $Z_{starter}$ = 0.46 ± 0.035 (n=7 samples) were normalized to $\theta'_{starter}$ = 1.00π and $Z'_{starter}$ = 0.490, respectively. In the histogram (Figure 2D, 6D, 7D, S2C, and S3D), individual bin size was 1/45 π for θ", and 0.02 for Z', except for Fig 7D top panels, where the bin sizes was 1/18 π for θ and 0.02 for Z.

Supplemental References

Berens, P. (2009). CircStat: A MATLAB Toolbox for Circular Statistics. J Stat Software *31*.

Brunjes, P.C., Illig, K.R., and Meyer, E.A. (2005). A field guide to the anterior olfactory nucleus (cortex). Brain Res Brain Res Rev *50*, 305-335.

Cohen, L., Rothschild, G., and Mizrahi, A. (2011). Multisensory integration of natural odors and sounds in the auditory cortex. Neuron *72*, 357-369.

Espinosa, J.S., Wheeler, D.G., Tsien, R.W., and Luo, L. (2009). Uncoupling dendrite growth and patterning: single-cell knockout analysis of NMDA receptor 2B. Neuron *62*, 205-217.

Hippenmeyer, S., Vrieseling, E., Sigrist, M., Portmann, T., Laengle, C., Ladle, D.R., and Arber, S. (2005). A developmental switch in the response of DRG neurons to ETS transcription factor signaling. PLoS Biology *3*, e159.

Huang, L., Garcia, I., Jen, H.I., and Arenkiel, B.R. (2013). Reciprocal connectivity between mitral cells and external plexiform layer interneurons in the mouse olfactory bulb. Frontiers Neural Circuits *7*, 32.

Kitamura, K., Judkewitz, B., Kano, M., Denk, W., and Häusser, M. (2008). Targeted patch-clamp recordings and single-cell electroporation of unlabeled neurons in vivo. Nat Methods *5*, 61-67.

Lepousez, G., Csaba, Z., Bernard, V., Loudes, C., Videau, C., Lacombe, J., Epelbaum, J., and Viollet, C. (2010). Somatostatin interneurons delineate the inner part of the external plexiform layer in the mouse main olfactory bulb. J Comp Neurology *518*, 1976-1994.

Luo, M., and Katz, L.C. (2001). Response correlation maps of neurons in the mammalian olfactory bulb. Neuron *32*, 1165-1179.

McCormick, D.A., Connors, B.W., Lighthall, J.W., and Prince, D.A. (1985). Comparative electrophysiology of pyramidal and sparsely spiny stellate neurons of the neocortex. J Neurophysi *54*, 782-806.

Miyamichi, K., Amat, F., Moussavi, F., Wang, C., Wickersham, I., Wall, N.R., Taniguchi, H., Tasic, B., Huang, Z.J., He, Z.*, et al.* (2011). Cortical representations of olfactory input by trans-synaptic tracing. Nature *472*, 191-196.

Niell, C.M., and Stryker, M.P. (2008). Highly selective receptive fields in mouse visual cortex. J Neurosci *28*, 7520-7536.

Reidl, J., Starke, J., Omer, D.B., Grinvald, A., and Spors, H. (2007). Independent component analysis of high-resolution imaging data identifies distinct functional domains. NeuroImage *34*, 94-108.

Rong, L., Gendron, K., Strohl, B., Shenoy, R., Wool-Lewis, R.J., and Bates, P. (1998). Characterization of determinants for envelope binding and infection in tva, the subgroup A avian sarcoma and leukosis virus receptor. J Virology *72*, 4552-4559.

Seidler, B., Schmidt, A., Mayr, U., Nakhai, H., Schmid, R.M., Schneider, G., and Saur, D. (2008). A Cre-loxP-based mouse model for conditional somatic gene expression and knockdown in vivo by using avian retroviral vectors. Proc Natl Acad Sci U S A *105*, 10137-10142.

Soucy, E.R., Albeanu, D.F., Fantana, A.L., Murthy, V.N., and Meister, M. (2009). Precision and diversity in an odor map on the olfactory bulb. Nat Neurosci. *12*, 210-220.

Tasic, B., Miyamichi, K., Hippenmeyer, S., Dani, V.S., Zeng, H., Joo, W., Zong, H., Chen-Tsai, Y., and Luo, L. (2012). Extensions of MADM (mosaic analysis with double markers) in mice. PloS One *7*, e33332.

Wall, N.R., Wickersham, I.R., Cetin, A., De La Parra, M., and Callaway, E.M. (2010). Monosynaptic circuit tracing in vivo through Cre-dependent targeting and complementation of modified rabies virus. Proc Natl Acad Sci U S A *107*, 21848-21853.

Watabe-Uchida, M., Zhu, L., Ogawa, S.K., Vamanrao, A., and Uchida, N. (2012). Whole-brain mapping of direct inputs to midbrain dopamine neurons. Neuron *74*, 858-873.

Wickersham, I.R., Lyon, D.C., Barnard, R.J., Mori, T., Finke, S., Conzelmann, K.K., Young, J.A., and Callaway, E.M. (2007). Monosynaptic restriction of transsynaptic tracing from single, genetically targeted neurons. Neuron *53*, 639-647.

Wickersham, I.R., Sullivan, H.A., and Seung, H.S. (2010). Production of glycoprotein-deleted rabies viruses for monosynaptic tracing and high-level gene expression in neurons. Nat Protoc *5*, 595-606.